

Contents lists available at ScienceDirect

Journal of Colloid and Interface Science

journal homepage: www.elsevier.com/locate/jcis



Benzoate anions-intercalated cobalt-nickel layered hydroxide nanobelts as high-performance electrode materials for aqueous hybrid supercapacitors



Yang Li ^{a,1}, Ziyang Luo ^{a,1}, Huizhen Qin ^a, Shunfei Liang ^a, Lingyun Chen ^{a,*}, Huayu Wang ^a, Chenglan Zhao ^a, Shaowei Chen ^{b,*}

HIGHLIGHTS

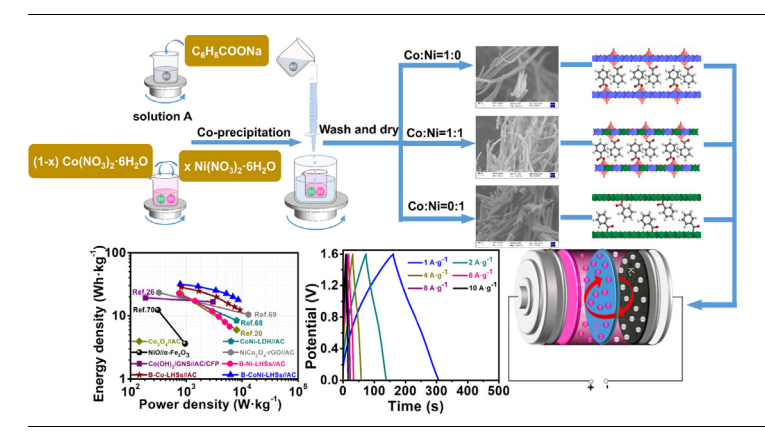
- One-dimensional B-CoNi-LHSs nanobelts were synthesized by using the co-precipitation method.
- The optimized electrode showed a high specific capacity of 570 $C \cdot g^{-1}$ at $1 \cdot A \cdot g^{-1}$.
- The B-CoNi-LHSs//AC device delivered a high energy density of 31.7 Wh·kg⁻¹ at power density of 780 W kg⁻¹.
- The device exhibited a remarkable cyclic stability (89.98% over 10,000 cycles).

ARTICLE INFO

Article history:
Received 18 June 2020
Revised 8 August 2020
Accepted 25 August 2020
Available online 29 August 2020

Keywords: Cobalt-nickel layered hydroxide Benzoate anions-intercalation Nanobelt Co-precipitation Supercapacitors

G R A P H I C A L A B S T R A C T



ABSTRACT

Layered metal hydroxide salts (LHSs) have recently gained extensive interests as an efficient electrode material for supercapacitors (SCs). Herein, we report, for the first time ever, the synthesis of a cobaltnickel layered hybrid organic-inorganic LHS that was intercalated with benzoate anions (B-CoNi-LHSs) and observe a high performance as electrode materials for hybrid supercapacitors (HSCs). B-CoNi-LHSs were synthesized by using a co-precipitation method, where sodium benzoate was added dropwise to cobalt and nickel salt solution, without the addition of any organic solvent or surfactant. Due to the intercalation of anions and synergistic interactions of the multi-metallic components, the B-CoNi-LHSs electrode showed a high specific capacity of 570 C g $^{-1}$ (specific capacitance of 1267 F·g $^{-1}$) at 1 A g $^{-1}$, excellent rate performance (65% from 1 to 10 A g $^{-1}$) and outstanding cycling performance (81.09% over 8000 cycles), in comparison to the mono-metallic counterparts. An HSC device, assembled by using B-CoNi-LHSs as the positive electrode and activated carbon (AC) as the negative one, exhibited a power density of 780 W kg $^{-1}$ at the energy density of 31.7 Wh kg $^{-1}$, and 8543 W kg $^{-1}$ at 18.1 Wh kg $^{-1}$. Results from this study show that the organic-inorganic hybrids of layered dual-metal hydroxides intercalated with benzoate anions may be a viable candidate as electrode materials for high-performance SCs.

© 2020 Elsevier Inc. All rights reserved.

^a School of Chemistry and Chemical Engineering, Chongqing University, Chongqing 400044, China

^b Department of Chemistry and Biochemistry, University of California, 1156 High Street, Santa Cruz, CA 95060, United States

^{*} Corresponding authors.

E-mail addresses: lychen@cqu.edu.cn (L. Chen), shaowei@ucsc.edu (S. Chen).

¹ These authors contributed equally to this work.

1. Introduction

With the ever-increasing consumption of non-renewable fossil fuels and the ensuing environmental issues, it has become imperative to explore clean, renewable, and highly efficient energy sources as well as the corresponding energy storage systems [1-3]. Among these, supercapacitors (SCs) have been recognized as one of the most promising candidates for energy storage, and the focus of a number of studies, due to their ultra-high power density, prominent cycle performance and fast charge-discharge rate, as compared to traditional batteries [4-7]. SCs have indeed found diverse applications, such as mobile electronics, hybrid electrical vehicles, etc. In order to achieve a high power density and energy density, hybrid supercapacitors (HSCs) are generally used with a boosted specific capacitance and expanded operating potential window [8-11], where the electrochemical performance is generally dictated by the chemical nature and structure of the electrode materials [4]. Towards this end, transition metal-based oxides and hydroxides (such as MnO₂ [12-15], Fe₂O₃ [16-19], Co₃O₄ [20], NiO [21], Co(OH)₂ [22,23], and Ni(OH)₂ [24]) have been extensively studied, because the specific capacitance is typically higher than that of traditional carbon-based electric double-layer capacitors (EDLC). It is well known that cobalt ions can be transformed into CoOOH with high conductivity, while Ni species can exhibit an ultra-high capacity due to its high activity and fast electron transfer [25]. By combining the advantages of these two metals, the deployment of cobalt-nickel hydroxides has indeed stimulated extensive research. In previous studies, Co- [20] and Ni-based [26,27] nanomaterials have shown a remarkable electrochemical performance, as compared with the Sn- [28-30], Cr- [31], and Znbased [32] counterparts. In addition, organic-inorganic hybrids based on layered metal hydroxides have been found to be effective electrode materials for SCs [33].

Layered metal hydroxides are generally divided into two categories. One is layered double hydroxides (LDHs) formed by the substitution of different-valence cations among the layers, with $[M_{1-x}^{2+}M_{x}^{3+}(OH)_{2}]A_{x/n}^{n-}MH_{2}O$, where M_{x}^{2+} and M_{x}^{3+} are divalent and trivalent metal cations at the octahedral sites, respectively, and A^{n-} is the interlayered anion to maintain a charge balance [34-36]. The other is the layered hydroxide metal salts (LHSs) formed by isotactic substitution of cations in the layer or substitution of part of the hydroxyl anions or water molecules, with the $[M^{2+}(OH)_{2-x}]A^{n-}_{x/n} \cdot mH_2O$, where M^{2+} is the metal ion (e.g., Co^{2+} , Ni^{2+} , Cu^{2+} , and Zn^{2+}), and A^{n-} is the counter ion (e.g., Cl^- , NO_3^- , SO_4^{2-} , CH_3COO^- , and $C_6H_5COO^-$) [37]. In recent years, LHSs intercalated with inorganic or organic anions, such as $Zn_5(OH)_8(NO_3)_2 \cdot 2H_2O$ [38], $\alpha - Cu_2(OH)_3Cl$ [39], Ni $(OH)_{1.4}(SO_4)_{0.3}$ [40], $Cu_2(OH)_3(CH_3COO) \cdot H_2O$ [41], Co(OH) $(C_6H_5COO)\cdot H_2O$ [42], and $Co(OH)_2$ -DS (DS = dodecyl sulfate) [43], have been attracting tremendous attention, due to its excellent electrochemical performance. However, intercalation of layered metal hydroxides with organic anions usually involve toxic organic solvents, surfactants and complicated operations, and no obvious improvement is observed of the electrochemical performance. Previous studies have shown that the introduction of interlayer anions with a large ionic radius is beneficial to increase the interlayer spacing of layered hydroxide, which helps expose active sites and enhance the electrochemical performance [44]. Therefore, intercalation of organic anions in a nonpolluting manner may be a viable strategy to prepare highperformance layered hydroxides. However, research in this area has been scarce.

Recently, multi-metallic LHSs have been adopted in order to increase the electrical conductivity due to the synergistic interactions between the metallic elements. LHSs with two metal $[M_y^a M^b_{1-y}(OH)_{2-x}] A^{n-}_{x/n} \cdot m H_2O$, where both metal centers are divalent cations [45]. Indeed, a series of double hydroxide salts (DHSs) have been prepared and studied, such as $Ni_{1/3}Co_{2/3}(CO_3)_{1/2}(OH)$.

 $0.11H_2O$ [46], NiCu(OH)_{3.1}(CH₃COO)_{0.9}·0.9H₂O [47], and Co_xNi_{1-x} (OH)(C₆H₅COO) [48]. However, few studies have focused on DHSs as electrode materials for SCs.

In this work, we use benzoate anions-intercalated cobalt-nickel layered hydroxide nanobelts as electrode material for HSCs. The samples were prepared by a facile co-precipitation method without the addition of organic solvents, surfactants or usage of expensive equipment, and displayed a high specific capacity of $570 \, \text{C g}^{-1}$ (specific capacitance of $1267 \, \text{F g}^{-1}$) at $1 \, \text{A g}^{-1}$, excellent rate performance (65% from 1 to $10 \, \text{A g}^{-1}$) and outstanding cycling performance (81.09% over 8000 cycles), in comparison to the mono-metallic counterparts. Furthermore, an HSCs based on B-CoNi-LHSs and activated carbon (AC) was found to deliver a high energy density of $31.7 \, \text{Wh kg}^{-1}$, maximum power density of $8543 \, \text{W kg}^{-1}$, as well as a durable cycle life (89.98% over $10,000 \, \text{cycles}$). This result indicates that DHSs intercalated with benzoate anions are a promising candidate of electrode materials for high-performance SCs.

2. Experimental section

2.1. Materials

Sodium benzoate (C_6H_5 COONa), cobalt nitrate hexahydrate ($Co(NO_3)_2 \cdot 6H_2O$), nickel nitrate hexahydrate ($Ni(NO_3)_2 \cdot 6H_2O$), potassium hydroxide (KOH), ethanol (C_2H_5OH) and polyvinylidene fluoride (PVDF) were purchased from Kelon in Chengdu. Foam nickel (NF) as a current collector was purchased from Jiayisheng Company. Commercial activated carbon (AC) was obtained from Nanjing Xianfeng Nano Material Technology Co., Ltd. All chemicals were of analytical grade and used with no further purification.

2.2. Sample preparation

B-Co-LHSs was synthesized by using a chemical co-precipitation method. In brief, 0.576 g of C_6H_5COONa was dissolved in 25 mL of an ethanol-water mixture (1:1 v/v) under magnetic stirring at room temperature to produce solution A. Separately, 0.582 g of $Co(NO_3)_2 \cdot 6H_2O$ was dispersed into an ethanol-water mixture (1:1 v/v) to form solution B. Solution A was then added into solution B in a dropwise manner under magnetic stirring for 24 h at 50 °C. The mixed solution was cooled to room temperature, and the pink suspension was centrifuged at 5000 rpm for 15 min. The obtained solid was washed several times with distilled water and ethanol, and dried in a vacuum oven for 24 h at 50 °C.

B-Ni-LHSs was prepared in the same procedur except that 0.582 g of Ni(NO₃)₂·6H₂O was used instead of Co(NO₃)₂·6H₂O. Similarly, B-CoNi-LHSs was produced by using 0.291 g of Co(NO₃)₂·6H₂O and 0.291 g of Ni(NO₃)₂·6H₂O.

2.3. Characterizations

X-ray diffraction (XRD) patterns were acquired on a Bruker D8 Advance powder diffractometer at 40 kV and 40 mA with Cu $\rm K_{\alpha}$ radiation (0.15406 nm). Morphology and size of the samples were examined with a HITACHI S-4800 field-emission scanning electron microscope (SEM) and a Tecnai G2 F20 S-Twin transmission electron microscope (TEM) operated at 200 kV. X-ray photoelectron spectroscopy (XPS) measurements were carried out with an ESCA-LAB250Xi spectrometer. Thermogravimetric analysis (TGA) was conducted with a Netzsch Luxx STA 409PC thermal analyzer within the temperature range of 30–800 °C at the heating rate of $10~\rm ^{\circ}C\cdot min^{-1}$ in a nitrogen flow.

2.4. Electrochemistry

Cyclic voltammetry (CV), galvanostatic charge-discharge (GCD) and electrochemical impedance spectroscopic (EIS) measurements were performed with a CHI 760E electrochemical workstation in a three-electrode configuration, which includes a reference electrode (saturated calomel electrode, SCE), a counter electrode (platinum electrode) and a working electrode in an aqueous electrolyte solution of 2 M KOH. The working electrode was a piece of nickel foam $(1 \times 1 \text{ cm}^2)$ coated with the active materials obtained above (ca. 1.5 mg cm⁻²), acetylene black and PVDF at a mass ratio of 80:10:10 using N-methyl 2-pyrrolidinone (NMP) as the solvent and fixed by a motor clamp. CV curves at different scan rates $(10-100 \text{ mV} \text{ s}^{-1})$ were obtained in the potential range of 0-0.6 V, and GCD curves at different current densities (1-10 A g⁻¹) were collected in the potential range of 0-0.45 V. EIS data was obtained in the frequency range of 0.01 Hz to 100 kHz at the open-circuit voltage. The cycling stability was tested using a LANHE test equipment. The specific gravimetric capacity ($Q_{sc,m}$, C g^{-1}) and specific gravimetric capacitance ($C_{sc,m}$, F g^{-1}) of the as-synthesized samples were calculated by the following equation [49]:

$$Q_{sc,m} = \frac{2I \int V \cdot dt}{m \cdot \Delta V} \tag{1}$$

$$C_{sc,m} = \frac{I \cdot \Delta t}{m \cdot \Delta V} \tag{2}$$

where I represents the current, ΔV the potential window, Δt the discharge time, m the mass load of the active material, and $\int V \, dt$ the integrated area enclosed by the discharge curve.

2.5. Hybrid supercapacitors

An HSC was assembled with B-M-LHSs as the positive and AC as the negative and the electrochemical performance was analyzed in a two-electrode system in 2 M KOH aqueous electrolyte solution. The optimal loading ratio of the active materials and AC was determined based on the following equation:

$$\frac{m^+}{m^-} = \frac{C^- \times \Delta V^-}{C^+ \times \Delta V^+} \tag{3}$$

where m, C and V denote the mass loading, specific capacity and potential window of the electrode materials, respectively, whereas superscripts + and - refer to the positive and negative electrode, respectively. The experimental performance was evaluated with the CHI 760E electrochemical workstation. The specific gravimetric capacity ($C_{HSC,m}$, mAh g $^{-1}$), gravimetric energy density (E, Wh kg $^{-1}$) and gravimetric power density (P, W kg $^{-1}$) were calculated according to the following equations:

$$C_{HSC,m} = \frac{2I \int V \cdot dt}{3.6m \cdot \Delta V} \tag{4}$$

$$E = \frac{I \int V \cdot dt}{3.6m} \tag{5}$$

$$P = \frac{3600 \times E}{\Delta t} \tag{6}$$

3. Results and discussion

The morphologies of the LHS samples were first examined by SEM and TEM measurements. It can be clearly seen from Fig. 1a and b that the as-obtained B-CoNi-LHSs was composed of long nanowire-like structures. High-magnification SEM images in Fig. 1c and d show that the sample actually consisted of

nanoribbons of around 110 nm in width. B-Co-LHSs (Fig. 1e-f) and B-Ni-LHSs (Fig. 1g-h) also show a nanoribbon structure, with the width between 100 and 200 nm (additional data are shown in Fig. S1). The TEM images are shown in Fig. 2. From Fig. 2a, it can be observed that the B-CoNi-LHSs sample indeed contained a large numer of densely packed and intertwined nanoribbons. The curvature suggests good flexibility of the nanobelts. The cross section of the rectangular nanoribbon can be observed in highmagnification TEM images (Fig. 2b), and the thickness of the nanoribbons can be estimated to be between 20 and 30 nm. Similar structures can be seen with B-Co-LHSs and B-Ni-LHSs (Fig. 2d-g). It can also be observed from Fig. 2e and g that the width of the nanoribbons is around 100 nm. Fig. 2c shows a high-resolution TEM image of the B-CoNi-LHSs nanoribbons. The sample can be seen to display clearly defined lattice fringes, with an interplanar distance of 1.48 nm and 0.75 nm corresponding to the (001) and (002) plane of B-CoNi-LHSs, which is consistent with results from XRD measurements [48].

Fig. 3 shows the layered structures of hybrid organic-inorganic B-Co-LHSs, B-Ni-LHSs and B-CoNi-LHSs. The coordination relationship between cobalt (Co^{II}) and hydroxide ion includes two types: octahedron (Co^{II}) and tetrahedron (Co^{II}), while nickel ion (Ni^{II}) and hydroxide ion only contain the octahedron (Ni^{II}) type [35,49-53]. The crystalline structures of the samples were examined by XRD measurements. From the XRD patterns in Fig. 4a, one can see that B-CoNi-LHSs, B-Co-LHSs and B-Ni-LHSs all exhibited three major diffraction peaks at $2\theta = 6.00^{\circ}$ (d = 1.48 nm), 11.90° (0.75 nm) and 17.85° (0.5 nm), corresponding to the (001), (002), and (003) crystal planes of Co(OH)(C₆H₅COO)·H₂O (JCPDS No. 42-1835) and Ni(OH)(C₆H₅COO)·H₂O (JCPDS No. 42-1836) [54], suggesting that these nanostructures consisted of two layers of benzoate anions stacked in the inner yer based on the size of the benzoate anion (0.7 nm) and the layer spacing (1.48 nm) of the LHSs [55]. In addition, the XRD diffraction peaks of B-CoNi-LHSs and B-Co-LHSs are highly similar, indicating the same crystal structure. Additionally, the low-intensity and broad features of the diffraction peaks suggest low crystallinity of the as-synthesized samples. Such disordering may be beneficial for the electrochemical performance [56].

XPS measurements were then carried out to examine the elemental compositions and valence states of the samples. Fig. 4b shows the survey spectra of B-M-LHSs, where the elements of Co, Ni, O, and C can be readily identified (C comes from the reference) [57]. Fig. 4c shows the high-resolution scan of the Co 2p electrons, where two pairs of peaks can be deconvolved at the binding energies (BEs) of 782.0/780.9 and 798.2/796.7 eV, ascribed to the 2p_{3/2} and $2p_{1/2}$ electrons of Co^{2+}/Co^{3+} , with two corresponding satellite peaks at 786.1 and 802.8 eV [58]. Similarly, from the highresolution scan of the Ni 2p electrons in Fig. 4d, the 2p_{3/2} and $2p_{1/2}$ electrons of Ni^{2+}/Ni^{3+} can be identified at 856.8/855.8 and 875.0/873.1 eV, with two shakeup satellites at 880.2 and 861.9 eV [59]. Fig. 4e is the high-resolution scan of the C 1s electrons. Two peaks can be resolved at 284.8 and 288.3 eV, corresponding to phenyl carbon and carboxylic group in the benzoate anion, respectively. In the O 1s spectrum (Fig. 4f), three peaks at 531.1, 531.6, and 532.5 eV can be resolved, due to the M-O, M—OH, and O—C=O in carboxyl groups, respectively [48,60]. Fig. S2 shows the high-resolution spectra of the other two monometallic systems. These results are consistent with the intercalation of benzoate ions into the LHS samples. Further thermal analysis was carried out by TGA measurements. From Fig. S3a, the first stage of weight loss (8.27%) can be seen to occur from 30 to 240 °C, due to the loss of water trapped in the as-obtained sample [34]. A second weight loss started at 240 °C, corresponding to the removal of hydroxyl groups and decomposition of the interlayer benzoate anion [61].

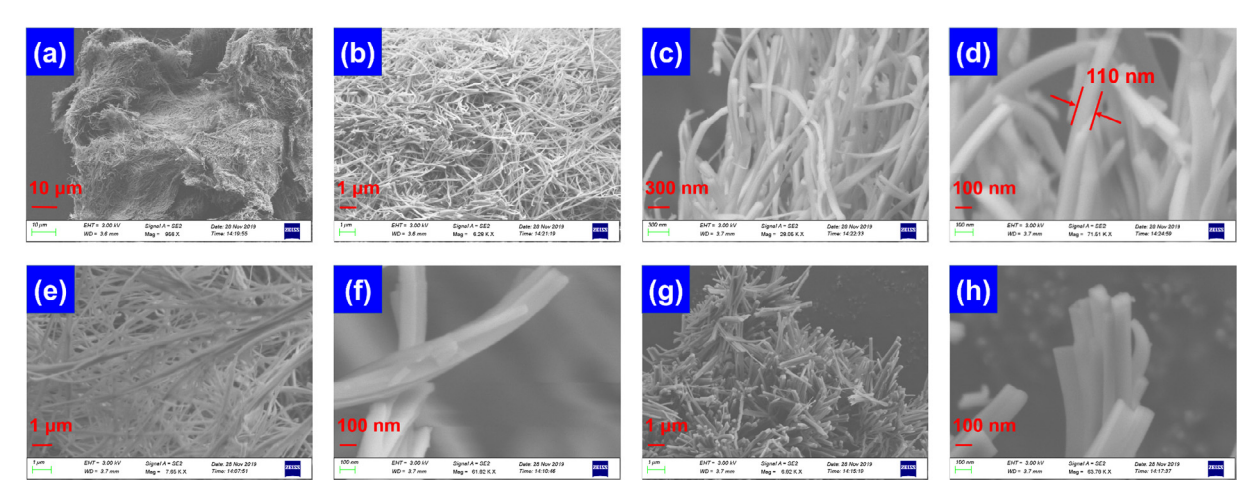


Fig. 1. SEM images of (a-d) B-CoNi-LHSs, (e-f) B-Co-LHSs, and (g-h) B-Ni-LHSs nanobelts.

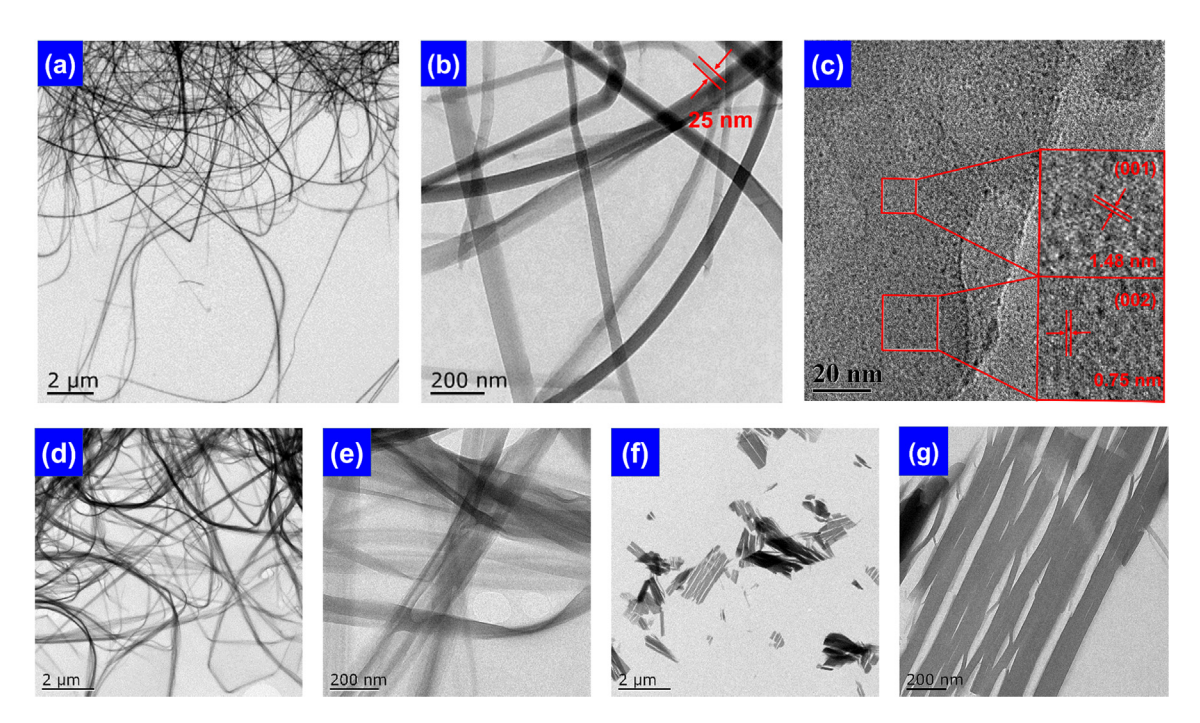


Fig. 2. TEM images of (a-c) B-CoNi-LHSs, (d-e) B-Co-LHSs, and (f-g) B-Ni-LHSs nanobelts.

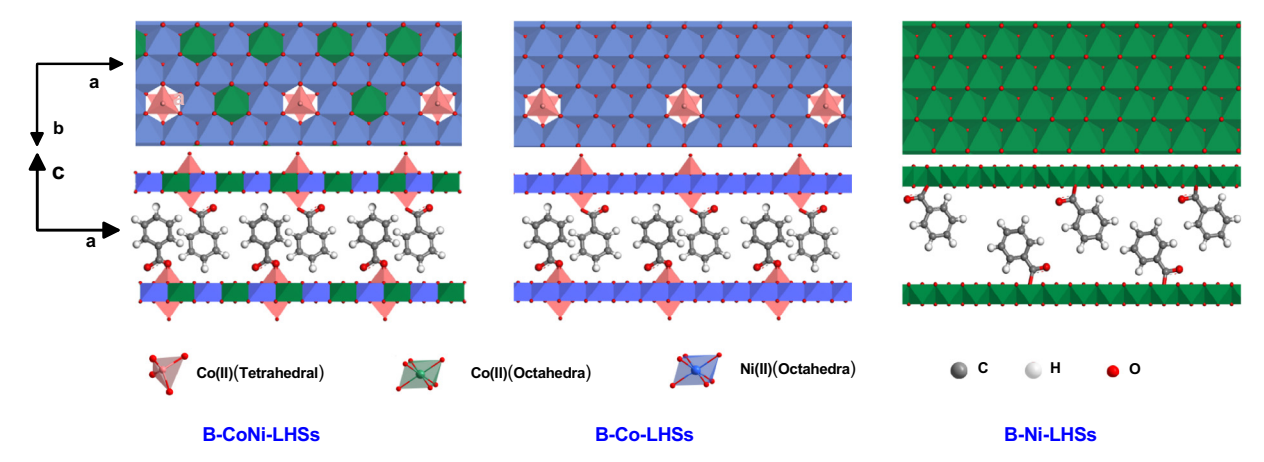


Fig. 3. Layered structures of hybrid organic-inorganic B-Co-LHSs, B-Ni-LHSs and B-CoNi-LHSs.

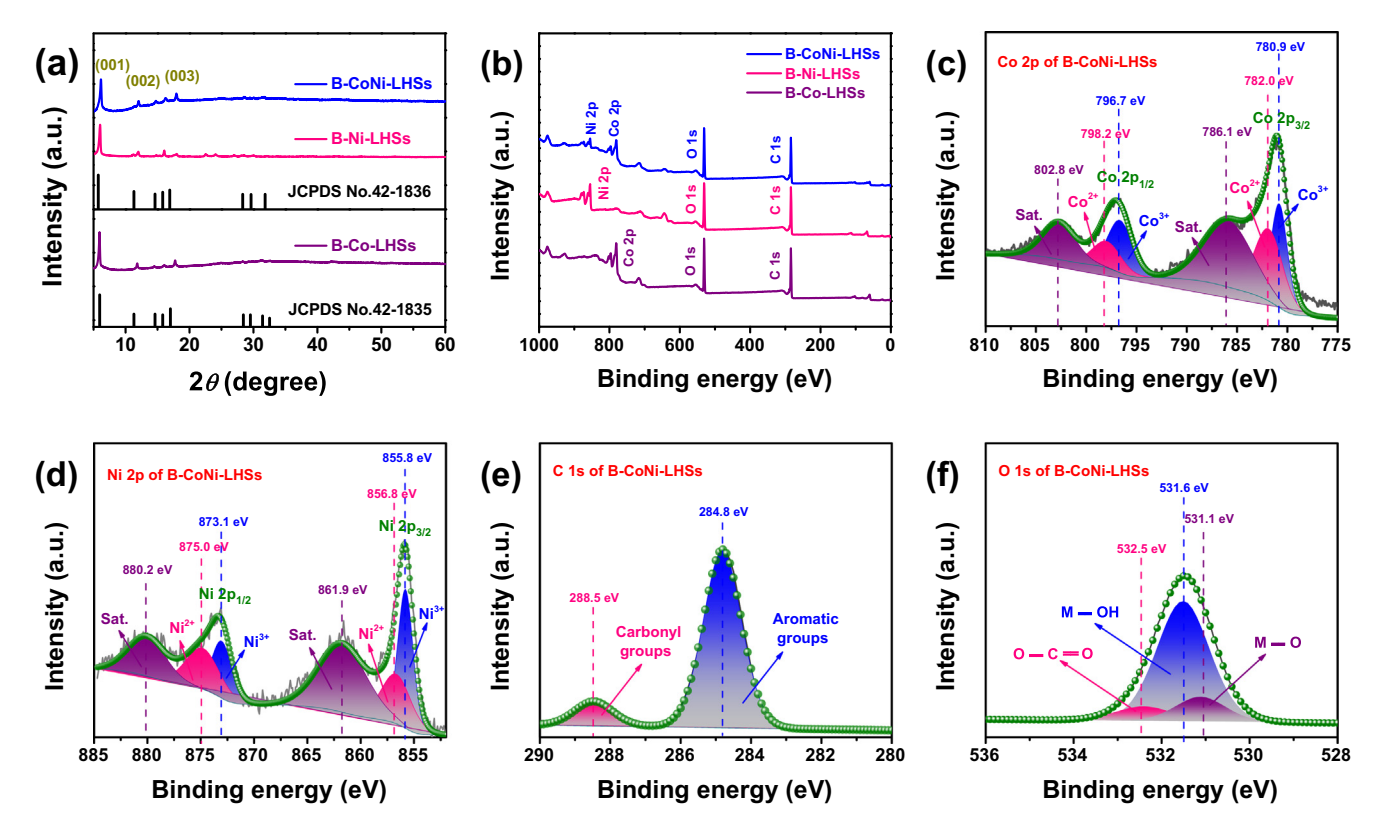


Fig. 4. (a) XRD patterns of B-M-LHSs, (b) XPS survey spectra, and high-resolution scans of the (c) Co 2p, (d) Ni 2p, (e) C 1s, and (f) O 1s electrons of B-CoNi-LHSs nanobelts.

The porosity of the material also plays a key role in high-performance SCs. The specific surface area (SSA) and pore size distribution of the B-CoNi-LHSs nanobelts were then evaluated using the nitrogen adsorption-desorption isotherm. Based on the IUPAC classification method, the B-CoNi-LHSs nanobelt isotherm curve (Fig. S3b) can be seen to exhibit a type IV isotherm with an obvious H3 hysteresis loop [62]. The inset to Fig. S3b shows the corresponding pore size distribution curve of the nanoribbons. The diameters of these pores are mostly concentrated between 3 and 50 nm, indicating the existence of a mesoporous structure in this sample. Its SSA, average pore size and pore volume are 31.6 m² g $^{-1}$, 3.37 nm and 0.139 m³ g $^{-1}$, respectively.

The electrochemical performances of the B-M-LHSs electrodes were then investigated by CV and GCD measurements in a conventional three-electrode setup in an aqueous electrolyte of 2 M KOH. Fig. 5a shows the CV curves of the three samples at the scan rate of 40 mV s $^{-1}$ within the potential window of 0–0.6 V (vs. SCE). It can be seen that all samples exhibited a battery-type behavior with a pair of redox peaks, which most likely arose from the faradaic reactions of the Ni and Co centers, namely, the Co $^{2+}$ /Co $^{3+}$, Co $^{3+}$ /Co $^{4+}$, and Ni $^{2+}$ /Ni $^{3+}$ couples [63,64].

When B replaces the benzoate anion, the possible chargedischarge mechanisms of B-M-LHSs can be explained by the following reactions [65]:

$$Co(II)(OH) - B + OH^{-} \leftrightarrow Co(III) - O - B + H_2O + e^{-}$$
(7)

$$Co(III) - O - B + OH^{-} \leftrightarrow Co(IV)(OH) - O - B + e^{-}$$
(8)

$$Ni(II)(OH) - B + OH^- \leftrightarrow Ni(III) - O - B + H_2O + e^-$$
 (9)

$$2Co_{0.5}(II)Ni_{0.5}(II)(OH) - B + 2OH^{-}$$

$$\leftrightarrow Co(III) - O - B + Ni(III) - O - B + 2H_{2}O + 2e^{-}$$
(10)

In addition, part of B-M-LHSs might be converted to Co(OH)₂ and Ni(OH)₂ during the charge-discharge process:

$$Co(II)(OH) - B + OH^{-} \leftrightarrow Co(II)(OH)_{2} + B^{-}$$
(11)

$$Co(II)(OH)_2 + OH^- \leftrightarrow Co(III)OOH + H_2O + e^-$$
 (12)

$$Co(III)OOH + OH^- \leftrightarrow Co(IV)O_2 + H_2O + e^-$$
(13)

$$Ni(II)(OH) - B + OH^- \leftrightarrow Ni(II)(OH)_2 + B^-$$
 (14)

$$Ni(II)(OH)_2 + OH^- \leftrightarrow Ni(III)OOH + H_2O + e^-$$
 (15)

$$2Co_{0.5}(II)Ni_{0.5}(II)(OH) - B + 2OH^{-}$$

$$\leftrightarrow Co(II)(OH)_{2} + Ni(II)(OH)_{2} + 2B^{-}$$
(16)

Additionally, from the integral area and peak currents of the three samples, B-CoNi-LHSs can be seen to exhibit a superior electrochemical performance, as compared to the other two monometallic samples, which may be attributed to the synergistic effect of multi-metallic system [66]. Fig. 5b shows the CV curves of the B-CoNi-LHSs electrode at various scan rates (10–100 mV s⁻¹) in the potential range of 0-0.6 V. It can be seen that as the scan rate increases, the cathodic and anodic peaks shifted to more positive and negative potentials, respectively [67], whereas the shape of the CV curves do not change signficantly, indicating that these electrodes have excellent reversibility. Furthermore, Fig. S4a and c depict the CV curves of the B-Co-LHSs and B-Ni-LHSs electrodes, respectively. Fig. 5c and Fig. S4 shows the linear relationship between the peak current (i) and the square root of the scan rate $(v^{1/2})$, which indicates that the electrochemical current of the samples are mainly diffusion-controlled [58]. It can be seen that the peak currents and integrated area of the B-CoNi-LHSs electrode

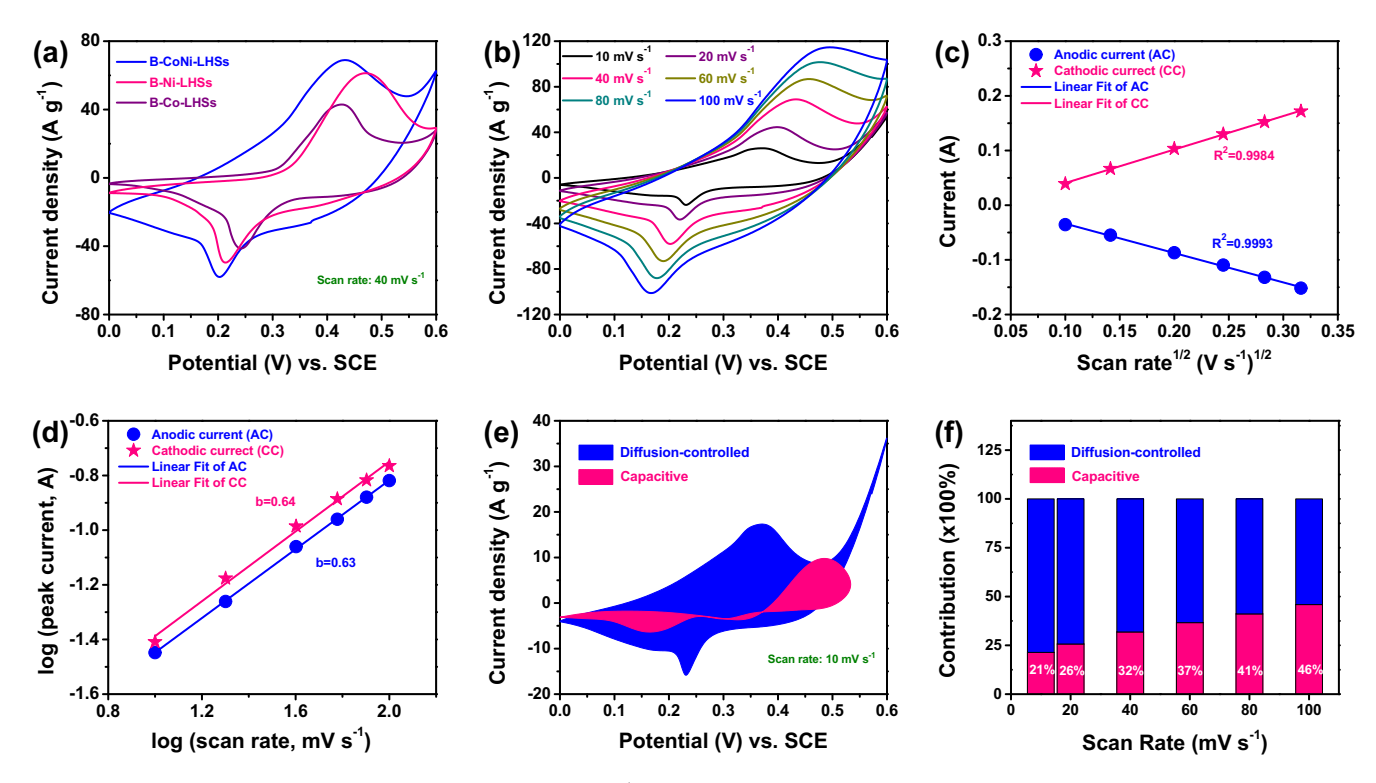


Fig. 5. (a) CV curves of B-M-LHSs electrodes at the same scan rate of $40 \text{ mV} \cdot \text{s}^{-1}$, (b) CV curves of the B-CoNi-LHSs electrode at various scan rates, (c) the variation of current of the cathodic and anodic peaks for the electrodes as a function of the square root of scan rate of B-CoNi-LHSs electrode, (d) linear relationship between fitted $\log(i)$ and $\log(v)$ of B-CoNi-LHSs electrode, (e) the contribution ratio of the capacitance effect and diffusion-controlled process to the total current of B-CoNi-LHSs electrode at $10 \text{ mV} \cdot \text{s}^{-1}$, respectively, (f) capacitance contribution ratio of B-CoNi-LHSs electrode at various scan rates.

are larger than the first two mono-metallic electrodes at a fixed scan rate, which indicates that the B-CoNi-LHSs electrode has the highest specific capacity.

To explore the capacitive effect of B-CoNi-LHSs, the relationship between the redox peak current (i) and different scan rates (v) was investigated by the following equation [68]:

$$i = a v^b \tag{17}$$

In order to further study the value of b, we take the logarithms on both sides of equation (17).

$$\log i = \log a + b \log v \tag{18}$$

$$b = \frac{\log i - \log a}{\log v} = \frac{\log i}{\log v} - \log_v a \ (constant) \tag{19}$$

Therefore, the value of b can be obtained by calculating the slope of the $\log(i)$ vs $\log(v)$ plot. When the value of b is equal to 1, it indicates that the kinetic reaction of the charge storage process is surface-controlled; while at the value of b is 0.5, it is diffusion-controlled [69]. Fig. 5d shows the relationship between $\log(i)$ and $\log(v)$ at different potentials. The values of b for the anodic and cathodic sweep were calculated by linear regression as 0.63 and 0.638, respectively, suggesting that the current was mainly diffusion-controlled. To further quantify the fraction of the diffusion-controlled component in the entire capacitance, we divide the current response i(V) at constant potential into two parts: capacitance effects (k_1v) and diffusion-controlled processes $(k_2v^{1/2})$, according to the following equation [70]:

$$i(V) = k_1 v + k_2 v^{1/2} (20)$$

For the convenience of analysis, we make a simple transformation of equation (20).

$$i(V)/v^{1/2} = k_1 v^{1/2} + k_2 (21)$$

Where the values of k_1 and k_2 can be determined by calculating the slope and intercept of the $i(V)/v^{1/2}$ vs $v^{1/2}$ plot, respectively. By fitting the CV data at different scan rates at a constant potential, the ratio of the diffusion-controlled process to the total current can be obtained. Fig. 5e depicts the area ratio of the diffusion-controlled process and the total current at the scan rate of 10 mV s⁻¹. Obviously, the capacitive effect accounts only for 21% of the total capacity, confirming that the current is indeed dominated by the diffusion-controlled process. To explore the changes in capacitance effects at different scan rates, Fig. 5f shows the capacitance process at higher scan rates. It can be seen that as the scan rate increases, the diffusion controlled contribution diminished gradually, because the electrolyte ions do not have enough time to enter the active material, resulting in restricted ion transport.

The GCD plots of all samples were measured at the current density of 4 A g⁻¹ and presented in Fig. 6a. All three GCD curves show outstanding symmetry of the plateau platform, which indicates highly reversible and extremely fast reaction kinetics [71]. This phenomenon is consistent with the results obtained from the CV measurements, demonstrating good supercapacitive behavior. Additionally, it can be seen that the B-CoNi-LHSs electrode showed a longer discharge time and a larger integrated area under the discharge plot than the other mono-metallic electrodes. Fig. 6b shows the GCD plots of the B-CoNi-LHSs at various current densities $(1-10 \text{ A g}^{-1})$ within the potential window of 0-0.45 V (vs. SCE). As the current densities increase, the diffusion of electrolyte ions on the B-CoNi-LHSs surface gradually weakens, which results in failure to fill the entire active material. Therefore, a completely sufficient redox reaction may not occur inside the material, which reduces the charge-discharge time and causes the reduction of the capacitance. According to equation (1) and (2), Q_{scm} and C_{scm}

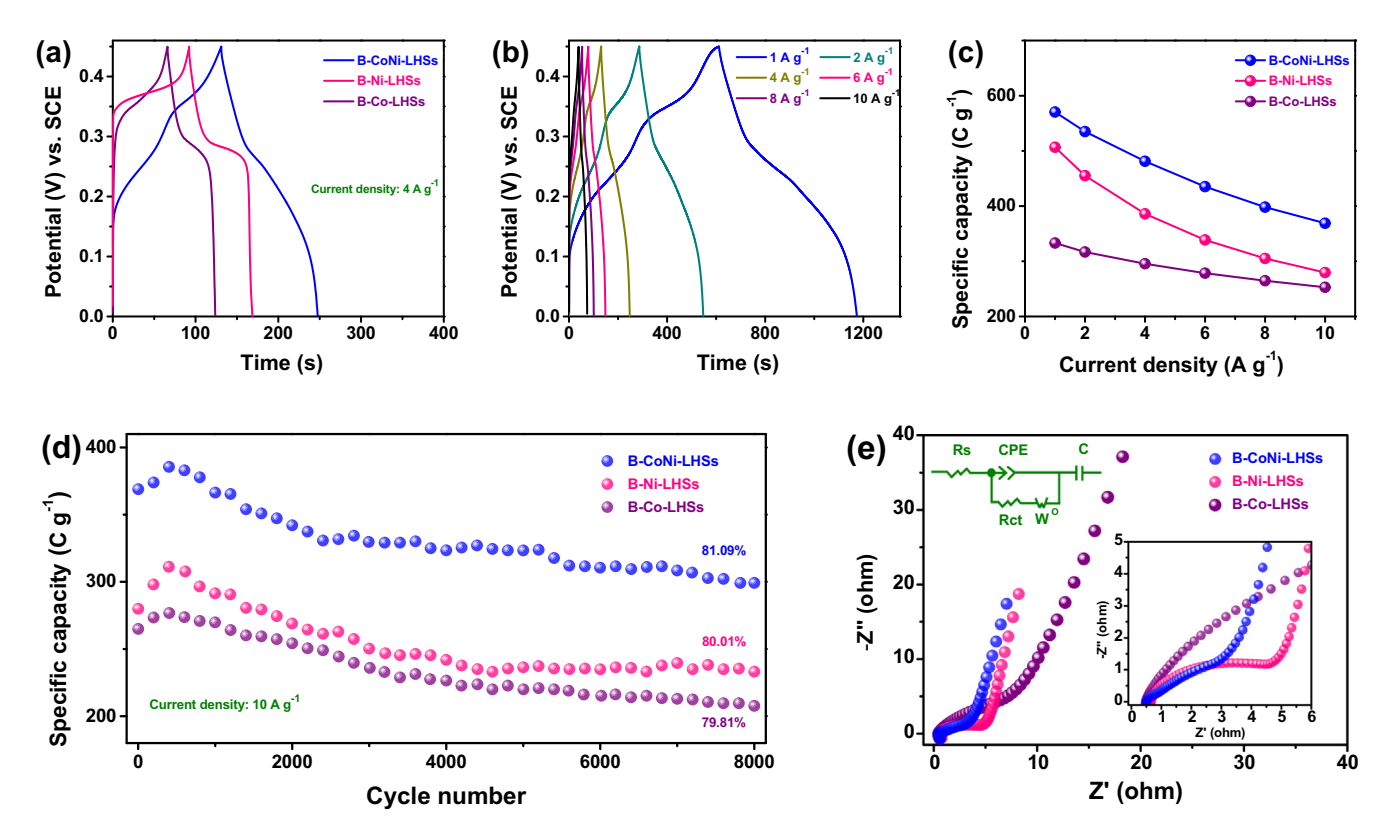


Fig. 6. (a) GCD curves of B-M-LHSs electrodes at the same current density of $4 \text{ A} \cdot \text{g}^{-1}$, (b) GCD curves of the B-CoNi-LHSs electrode at various current densities and (c) the calculated specific capacity at various current densities. (d) Cycling performance over 8000 GCD cycles at 10 A·g⁻¹ and (e) Nyquist plots of B-M-LHSs electrodes.

of the B-CoNi-LHSs electrode at a current density of 1, 2, 4, 6, 8, and 10 A g⁻¹ were calculated to be 570, 535, 481, 435, 398, and 369 C g^{-1} (1267, 1189, 1068, 967, 884, and 820 F g^{-1}), respectively, with a rate performance of 65% retention from 1 to 10 A g^{-1} . Meanwhile, the GCD plots $(1-10 \text{ A g}^{-1})$ of the other mono-metallic compounds were shown in Fig. S4. Using the same method, $Q_{sc,m}$ and $C_{sc,m}$ of the B-Co-LHSs electrode at a current density of 1, 2, 4, 6, 8, and 10 A $\rm g^{-1}$ were 333, 316, 295, 278, 265, and 253 C g^{-1} (740, 702, 656, 618, 589, and 562 F $\rm g^{-1}$), respectively, with 76% performance retention rate. $Q_{sc,m}$ and $C_{sc,m}$ of the B-Ni-LHSs electrode at a current density of 1, 2, 4, 6, 8, and 10 A g^{-1} were 507, 455, 386, 339, 305, and 280 C g^{-1} (1127, 1011, 858, 753, 678, and 622 F g^{-1}), respectively, with 55% performance retention rate. From Fig. 6c, one can see that the specific capacitance of the B-CoNi-LHSs electrode is higher than those of the mono-metallic electrodes at the same current density (1–10 ${\rm A~g^{-1}}$). In addition, as shown in many previous studies in Table 1 [43,46,60,72-82], the B-Ni-LHSs electrode exhibits superior electrochemical performance compared to the B-Co-LHSs electrode, which may be ascribed to the more facile faradaic process of the Ni centers than the Co ones [83,84].

The long-term stability is another important parameter in the evaluation of the electrochemical performance. Fig. 6d depicts the cyclic stability plots of the B-M-LHSs electrodes by constant current charge-discharge tests at 10 A g⁻¹ for 8000 cycles. After 8000 cycles, the capacity retention rate of the B-CoNi-LHSs (81.09%) electrode is slightly higher than those of B-Co-LHSs (79.81%) and B-Ni-LHSs (80.01%), suggesting excellent reversible response. In the first 600 cycles, the capacity retention of all three electrodes increased slightly, which was attributed to the activation of the electrode materials. During the activation process, electrolyte ions gradually penetrated into the active material, which provided an increasing number of active sites for redox reactions [85,86]. B-CoNi-LHSs exhibits outstanding cyclic stability due to

two important factors. One is the expansion of the layer spacing with the intercalation of benzoate anion into in the layered hydroxide, which is conducive to the transport and diffusion of ions. The other is the synergistic effect of the Co-Ni multimetallic system, which is beneficial to increase the electrical conductivity of the electrode system. In summary, B-CoNi-LHSs exhibits better electrochemical performance than the other two electrodes.

EIS measurements were then conducted to investigate the charge transfer kinetics of the three different electrodes. Fig. 6e shows the Nyquist plots of B-M-LHSs containing the internal resistance (R_s) and the charge transfer resistance (R_{ct}) . R_s is the intercept of the curve on the real axis, which is associated with the resistance of the electrolyte and the electrical component system. In the equivalent circuit shown, CPE is used instead of capacitor (C) [87-91]. The values of R_s are 0.596, 0.754, and 0.645 Ω cm² for B-Co-LHSs, B-Ni-LHSs, and B-CoNi-LHSs, respectively. In addition, R_{ct} is the diameter of the semicircle at a high frequency, which is related to the the faradaic process. The values of their R_{ct} are 2.369, 2.507, and 0.8837 Ω cm², respectively. Finally, the slope of the linear segment is the highest for B-CoNi-LHSs at low frequency, indicating fastest diffusion rate of OH⁻ [92]. These results indicate that the B-CoNi-LHSs stood out with the best performance among the three electrodes. This may be attributed to the synergistic effect of the multi-metallic system, which is conducive to the penetration and diffusion of electrolyte ions, enhancing the reaction kinetics.

To further explore the practical application of the as-prepared samples, HSC devices (denoted as B-M-LHSs//AC) were assembled by using the B-M-LHSs nanobelts as the positive electrode (B-M-LHSs/Ni foam) and AC as the negative electrode (AC/Ni foam) in 2 M KOH aqueous electrolyte (Fig. 7a). Before the assembly of devices, the electrochemical performance of AC was tested by

Table 1The comparison of the electrochemical property of various layered metal hydroxide.

Nano-structure	Specific capacitance (F g^{-1})	Rate performance	Cycle stability	Ref.
Co(CO ₃) _{0.5} (OH)/Ni ₂ CO ₃ (OH) ₂ nanobelt	987 (1 A g ⁻¹)	85% (from 1 to 10 A g ⁻¹)	82.9% (2000 cycles)	[72]
CrCu-N nanosheet (CrCu-LDH-NO ₃)	943 (1 A g ⁻¹)	19% (from 1 to 5 A g ⁻¹)	85% (1500 cycles)	[73]
MXene-Ni-Co-LDH nanosheet	$983.6 (2 \text{ A g}^{-1})$	55% (from 2 to 50 A g ⁻¹)	76% (5000 cycles)	[74]
CoNi-LDH nanosheet	$394.5 (1 \text{ A g}^{-1})$	54.5% (from 1 to 20 A g ⁻¹)	92.3% (10,000 cycles)	[60]
Co(OH) ₂ nanowires	$358 (0.5 \text{ A g}^{-1})$	90.7% (from 0.5 to 10 A g ⁻¹)	86.3% (5000 cycles)	[75]
$Co(OH)_2 -NO_3^-$	$582.7 (1 \text{ A g}^{-1})$	33.3% (from 1 to 8 A g ⁻¹)	62.5% (2000 cycles)	[43]
NCC/PNTs nanotubes	$964.8 (1 \text{ A g}^{-1})$	77.1% (from 1 to 20 A g ⁻¹)	=	[76]
NC-CNT-2 nanorods	1246.1 (0.5 A g ⁻¹)	92.1% (from 0.5 to 20 A g ⁻¹)	94% (10,000 cycles)	[46]
CF-Co(OH) _x CO ₃ microflowers.	550 (2 A g ⁻¹)	58.5% (from 2 to 5 A g ⁻¹)	99.5% (1500 cycles)	[77]
MnO ₂ /Ni(OH) ₂ nanosheet	843 (1 A g ⁻¹)	79.1% (from 0.1 to 5 A g ⁻¹)	79.1% (2000 cycles)	[78]
Ni _{0.5} Mg _{0.5} Co ₂ TMH nanosheet	$624 \text{ C g}^{-1} (10 \text{ A g}^{-1})$	59% (from 10 to 100 A g ⁻¹)	80% (3000 cycles)	[79]
Co ₃ Ni ₁ -LDHs@PCPs	1918 (1 A g ⁻¹)	81.3% (from 1 to 30 A g ⁻¹)	94.82% (10,000 cycles)	[80]
Ni-Co LDH on metal nickel	2184 (1 A g ⁻¹)	68.41% (from 1 to 20 A g ⁻¹)	88.5% (2000 cycles)	[81]
Ni-Co LDH	2682 (3 A g ⁻¹)	63.6% (from 3 to 20 A g ⁻¹)	_	[82]
B-CoNi-LHSs	1267 (570 C g ⁻¹) (1 A g ⁻¹)	65% (from 1 to 10 A g ⁻¹)	81.09% (8000 cycles)	This work

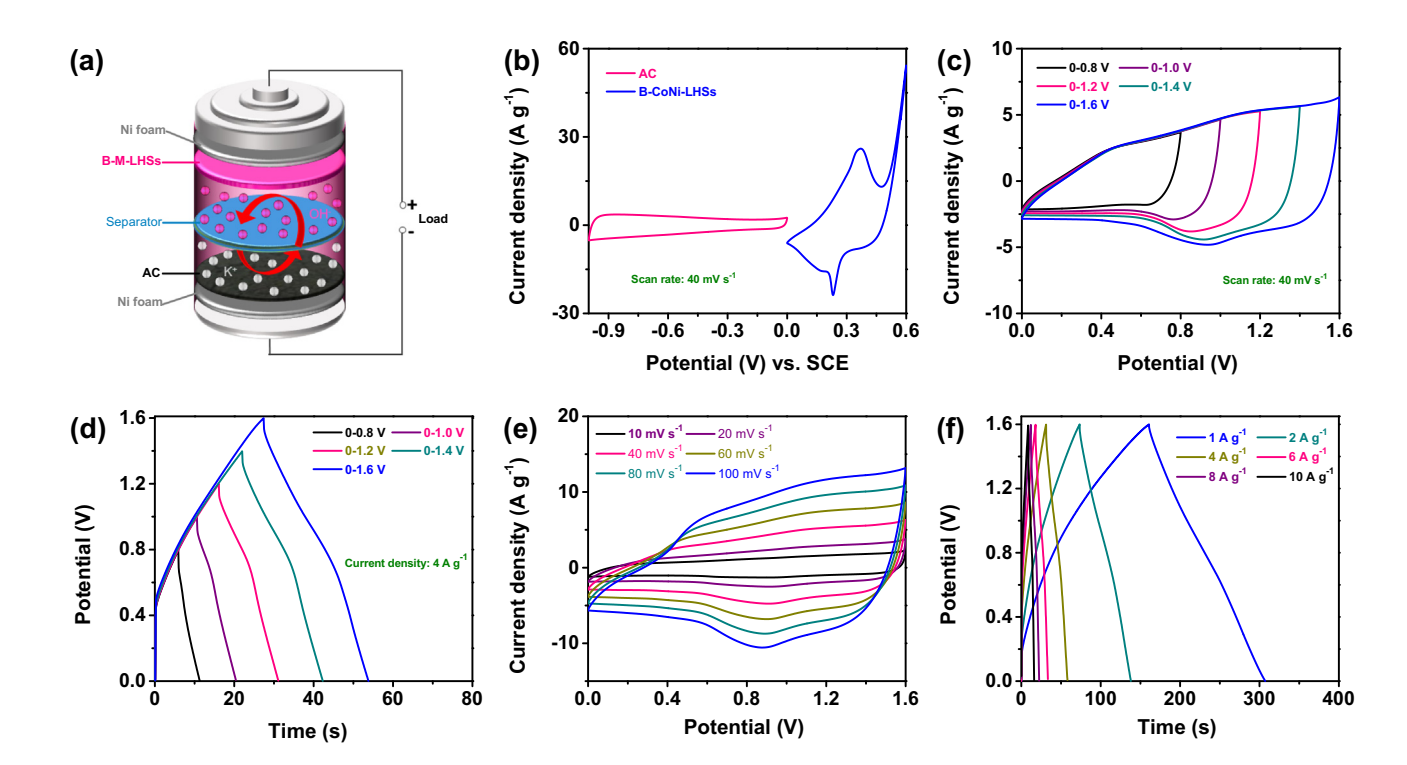
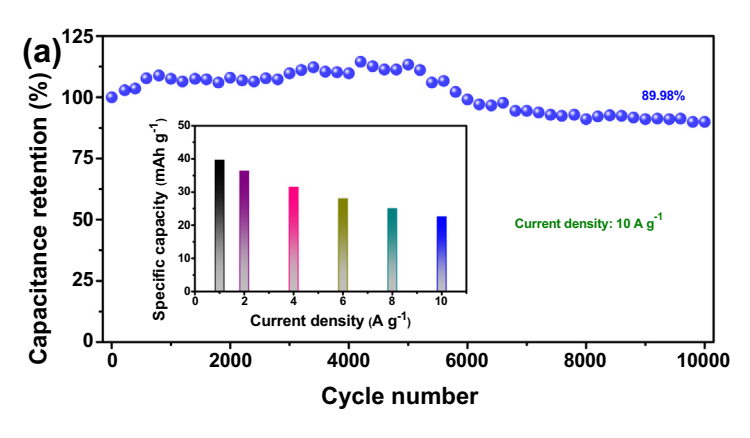


Fig. 7. (a) schematic illustration of the assembled B-M-LHSs//AC configuration, (b) CV curves of AC and B-CoNi-LHSs electrodes at the same scan rate of 40 mV·s $^{-1}$, (c) CV curves at a scan rate of 40 mV·s $^{-1}$ and (d) GCD curves at a current density of 4 A·g $^{-1}$ of the B-CoNi-LHSs//AC device in different voltage windows, (e) CV curves at different scan rates, and (f) GCD curves at different current densities of the B-CoNi-LHSs//AC device.

using a similar three-electrode system. Fig. S5 shows the CV curves of AC in a rectangular shape at various scan rates (10–100 mV s⁻¹) and the GCD curves of in a triangle shape at different current densities $(1-10 \text{ A g}^{-1})$, indicating that AC has typical EDLCs behavior. Fig. 7b shows the CV curves of the AC in the potential range of -1.0-0 V (vs. SCE) and B-CoNi-LHSs electrodes in the potential range of 0-0.6 V at the scan rate of 10 mV s⁻¹, respectively. It can be seen that the B-CoNi-LHSs//AC HSC exhibited a batterylike potential window of 0-1.6 V. To further verify the range of the potential window, Fig. 7c and d show the CV curves of the device at 40 mV s⁻¹ and the GCD curves of 4 A g⁻¹ between the potential window of 0-0.8 V and 0-1.6 V, respectively. When the potential is 1.6 V, the CV curve shows a slight polarization trend. Considering the stability and service life of the device, its ideal potential window was then set to 0-1.6 V. The CV curves of the B-CoNi-LHSs//AC device at various scan rates (10–100 mV s⁻¹) did show a redox couple (Fig. 7e), revealing that the assembled

device displayed pseudocapacitive behavior. At the same time, all GCD curves of the device at different current densities (1–10 A $\rm g^{-1}$, Fig. 7f) show a symmetrical triangle shape, indicating that the device has excellent reversibility and high coulombic efficiency. In addition, Fig. 8a depicts the cyclic stability curve of the device by constant current charge-discharge tests at 10 A $\rm g^{-1}$ for 10,000 cycles, which indicates a remarkable cyclic stability of 10.02% capacitance loss. In the inset to Fig. 8a, the $C_{HSC,m}$ of the device at a current density of 1, 2, 4, 6, 8, and 10 A $\rm g^{-1}$ were calculated as 39.6, 36.4, 31.4, 28.1, 25.1, and 22.5 mAh $\rm g^{-1}$, respectively, showing that the rate performance of 57% from 1 to 10 A $\rm g^{-1}$.

In order to compare the electrochemical performances of the three devices, the electrochemical performances of the B-Co-LHSs//AC and B-Ni-LHSs//AC devices were also examined (Fig. S6). The energy density (*E*) and power density (*P*) of the three devices are shown in Fig. 8b. From the Ragone plots, it can be seen that when the power density of the B-CoNi-LHSs//AC device



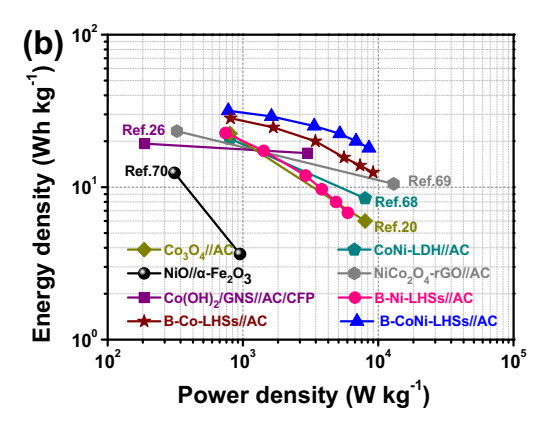


Fig. 8. (a) Cycling performance over 10,000 GCD cycles at 10 A·g⁻¹ of the B-CoNi-LHSs//AC device, and (b) Ragone Plot related to energy and power densities of the assembled B-M-LHSs//AC devices and other devices. The inset of the (a) shows the corresponding specific capacitances at different current densities of the B-CoNi-LHSs//AC device.

increased from 780 to 8543 W kg^{-1} , the energy density decreased from 31.7 to 18.1 Wh kg^{-1} , a performance better than those of B-Co-LHSs//AC (22.6 Wh kg^{-1} at 744 W kg^{-1} , and 6.8 Wh kg^{-1} at 5961 W kg⁻¹), and B-Ni-LHSs//AC (28.3 Wh kg⁻¹ at 811 W kg⁻¹, and 12.5 Wh kg⁻¹ at 9167 W kg⁻¹). The energy/power density of the B-CoNi-LHSs//AC device is also higher than those of some recently reported oxide- and hydroxide-based devices, such as $Co_3O_4//AC$ (22.49 Wh kg^{-1} at 800 W kg^{-1} , and 6 Wh kg^{-1} at 8000 W kg^{-1}) [20], $Co(OH)_2/GNS//AC/CFP$ (19.3 Wh kg^{-1} at 187.5 W kg^{-1} , and 16.7 Wh kg^{-1} at 3000 W kg^{-1}) [22], CoNi-LDH//AC (20.8 Wh kg⁻¹ at 800 W kg⁻¹, and 8.44 Wh kg⁻¹ at 8000 W kg⁻¹) [60], NiCo₂O₄-rGO//AC (23.3 Wh kg⁻¹ at 324.9 W kg $^{-1}$, and 10.5 Wh kg $^{-1}$ at 12,990 W kg $^{-1}$) [93], NiO// α -Fe₂O₃ (12.4 Wh kg $^{-1}$ at 312 W kg $^{-1}$, and 3.64 Wh kg $^{-1}$ at 951 W kg⁻¹) [94]. As can be seen from Fig. S7, the energy density of the B-CoNi-LHSs//AC device is much higher than those of electrochemical double layer capacitors and electrolytic capacitors. These results indicate that B-CoNi-LHSs nanobelts are promising candidates for high-performance SCs, which may be attributed to their layered structure with large interlayer spacing and the synergistic effect of the Co-Ni multi-metallic system.

4. Conclusions

In summary, we report, for the first time ever, the synthesis of layered hybrid organic-inorganic B-CoNi-LHSs nanobelts intercalated with benzoate anions by a facile co-precipitation method. The as-prepared products were characterized by a range of microscopic and spectroscopic measurements. The B-CoNi-LHSs sample was found to exhibit a high specific capacity of 570 C g⁻¹ (specific capacitance of 1267 F g^{-1}) at 1 A g^{-1} , excellent rate performance $(65\% \text{ from 1 to } 10 \text{ A g}^{-1})$ and better cycle performance (81.09% over)8000 cycles), as compared to other two mono-metallic systems. This was largely due to the intercalation with benzoate ions that increased the interlayer spacing of the hydroxides and facilitated the rapid diffusion of ions and enhanced exposure of the active sites. Interestingly, a B-CoNi-LHSs//AC HSC device was found to achieve achieve a wide operating voltage of 1.6 V and a high energy density of 31.7 Wh kg⁻¹ at a power density of 780 W kg⁻¹. These results confirmed that one-dimensional B-CoNi-LHSs nanobelts are promising candidates for SCs, and the strategy can be extended to other intercalating anions and transition metal-based layered metal hydroxides for further improvement of the capacitance performance.

CRediT authorship contribution statement

Yang Li: Investigation, Data curation, Writing - original draft. **Ziyang Luo:** Data curation, Investigation. **Huizhen Qin:** Validation,

Investigation. **Shunfei Liang:** Validation, Investigation. **Lingyun Chen:** Conceptualization, Supervision. **Huayu Wang:** Validation. **Chenglan Zhao:** Data curation. **Shaowei Chen:** Validation, Supervision.

Declaration of Competing Interest

The authors declare that they have no known competing financial interests or personal relationships that could have appeared to influence the work reported in this paper.

Acknowledgments

The authors gratefully acknowledge financial support from the National Natural Science Foundation of China (No. 21101176 and 21676036), the Fundamental Research Funds for the Central Universities of Chongqing University (No. 2018CDQYCH0028, 2018CDXYHG0028 and 2019CDXYHG0013), the Graduate Research and Innovation Foundation of Chongqing (No. CYS–18032), and the Large-scale Equipment Sharing Fund of Chongqing University (No. 201903150149 and 202003150020). S.W.C. thanks the National Science Foundation for partial support of the work (CHE-2003685 and CHE-1900235).

Appendix A. Supplementary material

Supplementary data to this article can be found online at https://doi.org/10.1016/j.jcis.2020.08.097.

References

- [1] E. Kim, E. Ahn, T. Dvir, D. Kim, Int. J. Nanomed. 9 (2014) 1-5.
- [2] S. Guo, S. Dong, Chem. Soc. Rev. 40 (2011) 2644–2672.
- [3] M. Pumera, Energ. Environ. Sci. 4 (2011) 668–674.
- [4] Y. Shao, M. Elkady, J. Sun, Y. Li, Q. Zhang, M. Zhu, H. Wang, B. Dunn, R. Kaner, Chem. Rev. 118 (2018) 9233–9280.
- [5] A. Forse, C. Merlet, J. Griffin, C. Grey, J. Am. Chem. Soc. 138 (2016) 5731–5744.
- [6] J. Liang, C. Jiang, W. Wu, Nanoscale 11 (2019) 7041-7061.
- [7] X. Zhao, L. Mao, Q. Cheng, J. Li, F. Liao, G. Yang, L. Xie, C. Zhao, L. Chen, Chem. Eng. J. 387 (2020) 124081.
- [8] X. Zhao, Q. Liu, Q. Li, L. Chen, L. Mao, H. Wang, S. Chen, Chem. Eng. J. 400 (2020) 125744.
- [9] D. Dubal, O. Ayyad, V. Ruiz, P. Gomezromero, Chem. Soc. Rev. 44 (2015) 1777– 1790.
- [10] J. Cherusseri, N. Choudhary, K. Kumar, Y. Jung, J. Thomas, Nanoscale Horiz. 4 (2019) 840–858.
- [11] J. Sun, C. Wu, X. Sun, H. Hu, C. Zhi, L. Hou, C. Yuan, J. Mater. Chem. A 5 (2017) 9443–9464.
- [12] L. Yuan, X. Lu, X. Xiao, T. Zhai, J. Dai, F. Zhang, B. Hu, X. Wang, L. Gong, J. Chen, ACS Nano 6 (2012) 656–661.
- [13] K. Kai, Y. Kobayashi, Y. Yamada, K. Miyazaki, T. Abe, Y. Uchimoto, H. Kageyama, J. Mater. Chem. 22 (2012) 14691–14695.
- [14] J. Zhu, J. He, ACS Appl. Mater. Inter. 4 (2012) 1770–1776.

- [15] Z. Wu, W. Ren, D. Wang, F. Li, B. Liu, H. Cheng, ACS Nano 4 (2010) 5835-5842.
- [16] S. Kumar, G. Saeed, N. Kim, J. Lee, J. Mater. Chem. A 6 (2018) 7182–7193.
- [17] Y. Zhu, S. Cheng, W. Zhou, J. Jia, L. Yang, M. Yao, M. Wang, J. Zhou, P. Wu, M. Liu, ACS Sustain. Chem. Eng. 5 (2017) 5067–5074.
- [18] L. Tian, M. Zhang, C. Wu, Y. Wei, J. Zheng, L. Lin, J. Lu, K. Amine, Q. Zhuang, F. Pan, ACS Appl. Mater. Inter. 7 (2015) 26284–26290.
- [19] Z. Ma, X. Huang, S. Dou, J. Wu, S. Wang, J. Phys. Chem. C 118 (2014) 17231– 17239.
- [20] J. Zhu, B. Huang, C. Zhao, H. Xu, S. Wang, Y. Chen, L. Xie, L. Chen, Electrochim. Acta 313 (2019) 194–204.
- [21] T. Kavitha, H. Yuvaraj, J. Mater. Chem. 21 (2011) 15686-15691.
- [22] C. Zhao, F. Ren, X. Xue, W. Zheng, X. Wang, L. Chang, J. Electroanal. Chem. 782 (2016) 98–102.
- [23] H. Sheng, X. Zhang, Y. Ma, P. Wang, J. Zhou, Q. Su, W. Lan, E. Xie, C. Zhang, ACS Appl. Mater. Inter. 11 (2019) 8992–9001.
- [24] B. Li, M. Zheng, H. Xue, H. Pang, Inorg. Chem. Front. 3 (2016) 175-202.
- [25] T. Chen, Y. Tang, W. Guo, Y. Qiao, S. Yu, S. Mu, L. Wang, Y. Zhao, F. Gao, Electrochim. Acta 212 (2016) 294–302.
- [26] S. Ede, S. Anantharaj, K. Kumaran, S. Mishra, S. Kundu, RSC Adv. 7 (2017) 5898–5911.
- [27] U. Nithiyanantham, S. Ede, S. Anantharaj, S. Kundu, Cryst. Growth. Des. 15 (2015) 673–686.
- [28] U. Nithiyanantham, A. Ramadoss, S. Kundu, Dalton T. 45 (2016) 3506-3521.
- [29] S. Ede, S. Kundu, ACS Sustain. Chem. Eng. 3 (2015) 2321-2336.
- [30] K. Sakthikumar, S. Ede, S. Mishra, S. Kundu, Dalton T. 45 (2016) 8897-8915.
- [31] J. Zhu, Y. Jiang, Z. Lu, C. Zhao, L. Xie, L. Chen, J. Duan, J. Colloid. Interf. Sci. 498 (2017) 351–363.
- [32] S. Ede, A. Ramadoss, U. Nithiyanantham, S. Anantharaj, S. Kundu, Inorg. Chem. 54 (2015) 3851–3863.
- [33] D. Zha, H. Sun, Y. Fu, X. Ouyang, X. Wang, Electrochim. Acta 236 (2017) 18–27.
- [34] X. Guo, L. Wang, S. Yue, D. Wang, Y. Lu, Y. Song, J. He, Inorg. Chem. 53 (2014) 12841–12847.
- [35] G. Rogez, C. Massobrio, P. Rabu, M. Drillon, Chem. Soc. Rev. 40 (2011) 1031– 1058.
- [36] G. Fan, F. Li, D. Evans, X. Duan, Chem. Soc. Rev. 43 (2014) 7040-7066.
- [37] G. Arizaga, K. Satyanarayana, F. Wypych, Solid State Ionics 178 (2007) 1143-
- [38] B. Hu, Z. Xue, H. Wang, L. Cai, H. Xiong, X. Jiang, Z. Du, J. Mater. Chem. 19 (2009) 2373–2379.
- [39] Y. Zhao, H. Cui, J. Zhang, Y. Ma, H. Tian, L. Wu, Q. Cui, Y. Ma, J. Phys. Chem. C 124 (2020) 9581–9590.
- [40] K. Zhang, J. Wang, X. Lu, L. Li, Y. Tang, Z. Jia, J. Phys. Chem. C 113 (2009) 142–147.
- [41] N. Masciocchi, E. Corradi, A. Sironi, G. Moretti, G. Minelli, P. Porta, J. Solid State Chem. 131 (1997) 252–262.
- [42] L. Huang, J. Jiang, L. Ai, ACS Appl. Mater. Inter. 9 (2017) 7059-7067.
- [43] L. Liu, J. Cheng, J. Zhang, F. Liu, X. Zhang, J. Alloy. Compd. 615 (2014) 868-874.
- [44] R. Ge, X. Ren, X. Ji, Z. Liu, G. Du, A. Asiri, X. Sun, L. Chen, ChemSusChem 10 (2017) 4004–4008.
- [45] F. Cao, G. Pan, P. Tang, H. Chen, J. Power Sources 216 (2012) 395–399.
- [46] W. Wei, S. Cui, L. Ding, L. Mi, W. Chen, X. Hu, ACS Appl. Mater. Inter. 9 (2017) 40655–40670.
- [47] N. Kozai, H. Mitamura, H. Fukuyama, F. Esaka, S. Komarneni, Micropor. Mesopor. Mat. 89 (2006) 123–131.
- [48] Y. Wang, L. Huang, L. Ai, M. Wang, Z. Fan, J. Jiang, H. Sun, S. Wang, Electrochim. Acta 318 (2019) 966–976.
- [49] S. Inoue, S. Fujihara, Inorg. Chem. 50 (2011) 3605–3612.
- [50] J. Demel, J. Hynek, P. Kovář, Y. Dai, C. Taviot-Guého, O. Demel, M. Pospíšil, K. Lang, J. Phys. Chem. C 118 (2014) 27131–27141.
- [51] L. Poul, N. Jouini, F. Fiévet, Chem. Mater. 12 (2000) 3123–3132.
- [52] L. Wang, Z. Dong, Z. Wang, F. Zhang, J. Jin, Adv. Funct. Mater. 23 (2013) 2758–
- [53] R. Rojas, Y. Linck, S. Cuffini, G. Monti, C. Giacomelli, Appl. Clay Sci. 109–110 (2015) 119–126.
- [54] K. Shrestha, S. Kandula, G. Rajeshkhanna, M. Srivastava, N. Kim, J. Lee, J. Mater. Chem. A 6 (2018) 24509–24522.
- [55] M. Ma, R. Ge, X. Ji, X. Ren, Z. Liu, A. Asiri, X. Sun, ACS Sustain. Chem. Eng. 5 (2017) 9625–9629.
- [56] H. Li, M. Yu, F. Wang, P. Liu, Y. Liang, J. Xiao, C. Wang, Y. Tong, G. Yang, Nat. Commun. 4 (2013) 1894.

- [57] G. Greczynski, L. Hultman, Angew. Chem. Int. Edit. 59 (2020) 5002-5006.
- [58] B. Huang, W. Wang, T. Pu, J. Li, C. Zhao, L. Xie, L. Chen, Chem. Eng. J. 375 (2019) 121969
- [59] B. Huang, H. Wang, S. Liang, H. Qin, Y. Li, Z. Luo, C. Zhao, L. Xie, L. Chen, Energy Storage Mater. (2020).
- [60] B. Huang, W. Wang, T. Pu, J. Li, J. Zhu, C. Zhao, L. Xie, L. Chen, J. Colloid. Interf. Sci. 532 (2018) 630–640.
- [61] J. Miao, M. Xue, H. Itoh, Q. Feng, J. Mater. Chem. 16 (2006) 474-480.
- [62] J. Zhu, D. Song, T. Pu, J. Li, B. Huang, W. Wang, C. Zhao, L. Xie, L. Chen, Chem. Eng. J. 336 (2018) 679–689.
- [63] J. Liang, C. Xiang, Y. Zou, X. Hu, H. Chu, S. Qiu, F. Xu, L. Sun, J. Mater. Sci. Technol. 55 (2020) 190–197.
- [64] D. Zhang, X. Guo, X. Tong, Y. Chen, M. Duan, J. Shi, C. Jiang, L. Hu, Q. Kong, J. Zhang, J. Alloy. Compd. 837 (2020).
 [65] Y. Zheng, S. Zheng, Y. Xu, H. Xue, C. Liu, H. Pang, Chem. Eng. J. 373 (2019)
- 1319-1328. [66] Y. Liu, X. Cao, L. Cui, Y. Zhong, R. Zheng, D. Wei, C. Barrow, J. Razal, W. Yang, J.
- Liu, J. Power Sources 437 (2019) 226897.
- [67] X. He, R. Li, J. Liu, Q. Liu, R. Chen, D. Song, J. Wang, Chem. Eng. J. 334 (2018) 1573–1583.
 [68] M. Zhang, H. Fan, X. Ren, N. Zhao, H. Peng, C. Wang, X. Wu, G. Dong, C. Long, W.
- [68] M. Zhang, H. Fan, X. Ren, N. Zhao, H. Peng, C. Wang, X. Wu, G. Dong, C. Long, W. Wang, Y. Gao, L. Ma, P. Wu, H. Li, X. Jiang, J. Power Sources 418 (2019) 202–210.
- [69] Y. Lu, Z. Li, Z. Bai, H. Mi, C. Ji, H. Pang, C. Yu, J. Qiu, Nano Energy 66 (2019) 104132.
- [70] W. Tian, H. Hu, Y. Wang, P. Li, J. Liu, J. Liu, X. Wang, X. Xu, Z. Li, Q. Zhao, H. Ning, W. Wu, M. Wu, ACS Nano 12 (2018) 1990–2000.
- [71] G. Rama Raju, E. Pavitra, G. Nagaraju, S. Sekhar, S. Ghoreishian, C. Kwak, J. Yu, Y. Huh, Y. Han, J. Mater. Chem. A 6 (2018) 13178–13190.
- [72] G. Zhang, P. Qin, R. Nasser, S. Li, P. Chen, J. Song, Chem. Eng. J. 387 (2020) 124029
- [73] A. Patil, J. Gunjakar, C. Lokhande, U. Patil, S. Sadavar, N. Padalkar, R. Shinde, M. Wagh, J. Bagi, Synthetic Met. 264 (2020) 116371.
- [74] H. Li, F. Musharavati, E. Zalenezhad, X. Chen, K. Hui, K. Hui, Electrochim. Acta 261 (2018) 178–187.
- [75] Y. Tang, Y. Liu, S. Yu, S. Mu, S. Xiao, Y. Zhao, F. Gao, J. Power Sources 256 (2014) 160–169.
- [76] Y. Wang, Y. Chen, Y. Liu, W. Liu, P. Zhao, Y. Li, Y. Dong, H. Wang, J. Yang, Electrochim. Acta 295 (2019) 989–996.
- [77] D. Ghosh, M. Mandal, C. Das, Langmuir 31 (2015) 7835-7843.
- [78] Z. Wang, F. Wang, J. Tu, D. Cao, X. An, Y. Ye, Mater. Lett. 171 (2016) 10–13.[79] A. Nanwani, K. Deshmukh, C. Subramaniyam, A. Deshmukh, J. Energy Storage
- 31 (2020) 101604.
- [80] W. Wang, Y. Lu, M. Zhao, R. Luo, Y. Yang, T. Peng, H. Yan, X. Liu, Y. Luo, ACS Nano 13 (2019) 12206–12218.
- [81] X. Zheng, Z. Gu, Q. Hu, B. Geng, X. Zhang, RSC Adv. 5 (2015) 17007–17013.[82] H. Chen, L. Hu, M. Chen, Y. Yan, L. Wu, Adv. Funct. Mater. 24 (2014) 934–942.
- [83] Y. Cheng, H. Zhang, C. Varanasi, J. Liu, Energ. Environ. Sci. 6 (2013) 3314–3321.
- [84] H. Chen, J. Jiang, Y. Zhao, L. Zhang, D. Guo, D. Xia, J. Mater. Chem. A 3 (2015)
- 428–437. [85] W. Lu, J. Shen, P. Zhang, Y. Zhong, Y. Hu, X. Lou, Angew. Chem. Int. Edit. 58
- (2019) 15441–15447. [86] G. He, J. Li, W. Li, B. Li, N. Noor, K. Xu, J. Hu, I. Parkin, J. Mater. Chem. A 3 (2015)
- 14272–14278. [87] H. Mohammad Shiri, A. Ehsani, M. Jalali Khales, J. Colloid. Interf. Sci. 505 (2017)
- 940–946. [88] A. Ehsani, M. Bigdeloo, M. Ansari, B. Mirtamizdoust, A. Heidari, M. Hadi, H.
- Shiri, B. Chem, Soc. Japan 91 (2018) 617–622. [89] H. Mohammad Shiri, A. Ehsani, R. Behjatmanesh-Ardakani, J. Taiwan Inst.
- (89) H. Mohammad Shiri, A. Ensam, R. Benjathianesh-Ardakani, J. Taiwan inst. Chem. E. 93 (2018) 632–643.
- [90] A. Ehsani, M. Bigdeloo, F. Assefi, M. Kiamehr, R. Alizadeh, Inorg. Chem. Commun. 115 (2020) 107885.
- [91] A. Ehsani, H. Parsimehr, H. Nourmohammadi, R. Safari, S. Doostikhah, Polym. Composite. 40 (2019) 4629–4637.
- [92] M. Li, K. Ma, J. Cheng, D. Lv, X. Zhang, J. Power Sources 286 (2015) 438–444.
- [93] X. Wang, W. Liu, X. Lu, P. Lee, J. Mater. Chem. 22 (2012) 23114–23119.
- [94] S. Zhang, B. Yin, Z. Wang, F. Peter, Chem. Eng. J. 306 (2016) 193–203.